Spectra of particulate backscattering in natural waters.

Howard R. Gordon[1,*], Marlon R. Lewis[2,3], Scott D. McLean[3], Michael S. Twardowski[4], Scott A. Freeman[4], Kenneth J. Voss[1], and G. Chris Boynton[1]

[1]*Department of Physics, University of Miami, Coral Gables, FL 33124, USA*
[2]*Department of Oceanography, Dalhousie University, Halifax, NS, B3H4J1, Canada*
[3]*Satlantic, Inc., Pier 9, Richmond Terminals, Halifax, NS, B3K5X8, Canada*
[4]*Department of Research, WET Labs, Inc., Narragansett, RI 02882, USA*
**hgordon@miami.edu*

Abstract: Hyperspectral profiles of downwelling irradiance and upwelling radiance in natural waters (oligotrophic and mesotrophic) are combined with inverse radiative transfer to obtain high resolution spectra of the absorption coefficient (a) and the backscattering coefficient (b_b) of the water and its constituents. The absorption coefficient at the mesotrophic station clearly shows spectral absorption features attributable to several phytoplankton pigments (Chlorophyll *a*, *b*, *c*, and Carotenoids). The backscattering shows only weak spectral features and can be well represented by a power-law variation with wavelength (λ): $b_b \sim \lambda^{-n}$, where n is a constant between 0.4 and 1.0. However, the weak spectral features in b_b suggest that it is depressed in spectral regions of strong particle absorption. The applicability of the present inverse radiative transfer algorithm, which omits the influence of Raman scattering, is limited to $\lambda < 490$ nm in oligotrophic waters and $\lambda < 575$ nm in mesotrophic waters.

OCIS codes: (010.4450) Oceanic optics; (010.4588) Oceanic scattering; (010,5620) Radiative transfer; (280.4991) Passive remote sensing.

References and links

1. G. J. Kirkpatrick, D. F. Millie, M. A. Moline, and O. Schofield, "Optical discrimination of a phytoplankton species in natural mixed populations," Limnol. Oceanogr. **45**, 467–471 (2000).
2. N. Hoepffner, and S. Sathyendranath, "Determination of major groups of phytoplankton pigments from absorption spectra of total particulate matter," J. Geophys. Res. **98**(C12 C12), 22789–22803 (1993).
3. C. O. Davis, J. Bowles, R. A. Leathers, D. Korwan, T. V. Downes, W. A. Snyder, W. J. Rhea, W. Chen, J. Fisher, P. Bissett, and R. A. Reisse, "Ocean PHILLS hyperspectral imager: design, characterization, and calibration," Opt. Express **10**(4), 210–221 (2002).
4. H. R. Gordon, and A. Y. Morel, *Remote Assessment of Ocean Color for Interpretation of Satellite Visible Imagery: A Review* (Springer-Verlag, 1983).
5. H. R. Gordon, and G. C. Boynton, "Radiance-irradiance inversion algorithm for estimating the absorption and backscattering coefficients of natural waters: vertically stratified water bodies," Appl. Opt. **37**(18), 3886–3896 (1998).
6. G. C. Boynton, and H. R. Gordon, "An irradiance inversion algorithm for absorption and backscattering profiles in natural waters: improvement for clear waters." Appl. Opt. **41**, 2224–2227 (2002).
7. C. D. Mobley, *Light and Water; Radiative Transfer in Natural Waters* (Academic Press, 1994).
8. K. M. Case, and P. F. Zweifel, *Linear Transport Theory* (Addison-Wesley, 1967).
9. H. R. Gordon, "The sensitivity of radiative transfer to small-angle scattering in the ocean: A quantitative assessment," Appl. Opt. **32**(36), 7505–7511 (1993).
10. S. Hooker, S. McLean, J. Sherman, M. Small, G. Lazin, G. Zibordi, and J. Brown, "The seventh SeaWiFS intercalibration round robin experiment (SIRREX-7)," NASA Technical Memorandum 2002–206892, Vol 17, SeaWiFS Postlaunch Technical Report Series (1999).
11. J. Mueller, C. Pietras, S. Hooker, R. Austin, M. Miller, K. Knobelspiesse, R. Frouin, B. Holben, and K. Voss, "Ocean optics protocols for satellite ocean color sensor validation, Revision 4, Volume 2: Instrument specifications, characterization, and calibration," NASA-TM-2003–21621/Rev4-Vol II, (2003).

#113277 - $15.00 USD Received 24 Jun 2009; revised 14 Aug 2009; accepted 21 Aug 2009; published 27 Aug 2009

12. M. S. Twardowski, J. M. Sullivan, P. L. Donaghay, and J. R. V. Zaneveld, "Microscale quantification of the absorption by dissolved and particulate material in coastal waters with an ac-9," J. Atmos. Ocean. Technol. **16**(6), 691–707 (1999).
13. W. S. Pegau, D. Gray, and J. R. V. Zaneveld, "Absorption and attenuation of visible and near-infrared light in water: dependence on temperature and salinity," Appl. Opt. **36**(24), 6035–6046 (1997).
14. J. M. Sullivan, M. S. Twardowski, J. R. V. Zaneveld, C. M. Moore, A. H. Barnard, P. L. Donaghay, and B. Rhoades, "Hyperspectral temperature and salt dependencies of absorption by water and heavy water in the 400-750 nm spectral range," Appl. Opt. **45**(21), 5294–5309 (2006).
15. J. R. V. Zaneveld, J. C. Kitchen, and C. M. Moore, "The scattering error correction of reflecting-tube absorption meters," Proc. SPIE **2258**, 44–55 (1994).
16. D. McKee, J. Piskozub, and I. Brown, "Scattering error corrections for in situ absorption and attenuation measurements," Opt. Express **16**(24), 19,480–19,492 (2008).
17. M. S. Twardowski, S. Freeman, X. Zhang, S. Vagle, and R. Zaneveld, "Resolving surf zone particle dynamics with high sampling rate volume scattering function measurements," Proc. Ocean Optics XIX, October 6–9, Barga, Italy (2008).
18. M. S. Twardowski, H. Claustre, S. A. Freeman, D. Stramski, and Y. Huot, ""Optical backscattering properties of the "clearest" natural waters," Biogeosciences **4**, 1041–1058 (2007).
19. C. Moore, M. S. Twardowski, and J. R. V. Zaneveld, "The ECO VSF - A multi-angle scattering sensor for determination of the volume scattering function in the backward direction," Proc. Ocean Optics XV, 16–20 October, Monaco, Office of Naval Research, USA (2000).
20. X. Zhang, and L. Hu, "Estimating scattering of pure water from density fluctuation of the refractive index," Opt. Express **17**(3), 1671–1678 (2009).
21. X. Zhang, L. Hu, and M.-X. He, "Scattering by pure seawater: effect of salinity," Opt. Express **17**(7), 5698–5710 (2009).
22. T. Oishi, "Significant relationship between the backward scattering coefficient of sea water and the scatterance at 120°," Appl. Opt. **29**(31), 4658–4665 (1990).
23. E. Boss, and W. S. Pegau, "Relationship of light scattering at an angle in the backward direction to the backscattering coefficient," Appl. Opt. **40**(30), 5503–5507 (2001).
24. J. M. Sullivan, M. S. Twardowski, P. L. Donaghay, and S. A. Freeman, "Use of scattering to discriminate particle types in Coastal Waters," Appl. Opt. **44**, 1667–1680 (2005).
25. J.-F. Berthon, E. Shybanov, M. E.-G. Lee, and G. Zibordi, "Measurements and modeling of the volume scattering function in the coastal northern Adriatic Sea," Appl. Opt. **46**(22), 5189–5203 (2007).
26. T. J. Petzold, "Volume scattering functions for selected natural waters," Scripps Institution of Oceanography, Visibility Laboratory, San Diego, CA. 92152, SIO Ref. 72–78 (1972).
27. F. M. Sogandares, and E. S. Fry, "Absorption spectrum (340-640 nm) of pure water. I. Photothermal measurements," Appl. Opt. **36**(33), 8699–8709 (1997).
28. R. M. Pope, and E. S. Fry, "Absorption spectrum (380-700 nm) of pure water. II. Integrating cavity measurements," Appl. Opt. **36**(33), 8710–8723 (1997).
29. A. Morel, B. Gentili, H. Claustre, M. Babin, A. Bricaud, J. Ras, and F. Tieche, "Optical properties of the 'clearest' natural waters," Limnol. Oceanogr. **52**, 217–239 (2007).
30. S. Maritorena, D. A. Siegel, and A. R. Peterson, "Optimization of a semianalytical ocean color model for global-scale applications," Appl. Opt. **41**(15), 2705–2714 (2002).
31. R. H. Stavn, and A. D. Weidemann, "Optical Modeling of Clear Ocean Light Fields: Raman Scattering Effects," Appl. Opt. **27**(19), 4002–4011 (1988).
32. B. R. Marshall, and R. C. Smith, "Raman scattering and in-water ocean optical properties," Appl. Opt. **29**(1), 71–84 (1990).
33. Y. Ge, K. J. Voss, and H. R. Gordon, "In situ measurements of inelastic light scattering in Monterey Bay using solar Fraunhofer lines," J. Geophys. Res. **100**(C7), 13,227–13,236 (1995).
34. H. R. Gordon, "Contribution of Raman scattering to water-leaving radiance: a reexamination," Appl. Opt. **38**(15), 3166–3174 (1999).
35. J. S. Bartlett, K. J. Voss, S. Sathyendranath, and A. Vodacek, "Raman scattering by pure water and seawater," Appl. Opt. **37**(15), 3324–3332 (1998).
36. A. Bricaud, A. Morel, and L. Prieur, "Optical efficiency factors of some phytoplankters," Limnol. Oceanogr. **28**, 816–832 (1983).
37. A. Morel, B. Gentili, M. Chami, and J. Ras, "Bio-optical properties of high chlorophyll Case 1 waters and of yellow-substance-dominated Case 2 waters," Deep Sea Res. Part I Oceanogr. Res. Pap. **53**(9), 1439–1459 (2006).
38. H. C. van de Hulst, "*Light scattering by small particles*," (Dover Publications, 1981).
39. J. R. V. Zaneveld, and J. Kitchen, "The variation in the inherent optical properties of phytoplankton near an absorption peak as determined by various models of cell structure," J. Geophys. Res. **100**(C7 C7), 13,309–13,320 (1995).
40. H. R. Gordon, and G. C. Boynton, "Radiance-irradiance inversion algorithm for estimating the absorption and backscattering coefficients of natural waters: homogeneous waters," Appl. Opt. **36**(12), 2636–2641 (1997).
41. H. R. Gordon, "Inverse Methods in Hydrologic Optics," Oceanologia **44**, 9–58 (2002).

#113277 - $15.00 USD Received 24 Jun 2009; revised 14 Aug 2009; accepted 21 Aug 2009; published 27 Aug 2009

1. Introduction

Space-borne sensors such as the Coastal Zone Color Scanner (CZCS), the Sea-viewing Wide Field-of-view Sensor (SeaWiFS), and the MODerate resolution Imaging Spectroradiometer (MODIS) have provided ocean color imagery from which the concentration of the phytoplankton photosynthetic pigment chlorophyll *a* (Chl *a*) has been estimated on a global scale since 1978. Phytoplankton are the first link in the marine food chain and play a significant role in the global carbon cycle and upper ocean heating. CZCS was a four-band radiometer operating from 443 to 670 nm, while SeaWiFS and MODIS are eight-band radiometers operating from 412 to 865 nm. It is reasonable to expect that an instrument with a larger number of spectral bands might provide more information regarding phytoplankton. For example, with a more detailed rendition of the ocean color spectrum it should be possible to apply advanced spectroscopic tools such as derivative analysis to determine the relative concentrations of the various accessory pigments; this would provide information regarding the size and species composition of the phytoplankton community [1]. Laboratory measurements clearly show spectral features that enable modeling of the plankton absorption with individual pigment components [2], suggesting that remote measurements could do the same. Indeed, "hyperspectral" reflectance measurements might enable a wide range of spectroscopic analyses of absorption and backscattering spectra to derive the phytoplankton species composition or community structure, an important determinant of the upper ocean carbon cycle and something that is not possible with the limited number of spectral channels available on most current satellite sensors. Such hyperspectral aircraft instruments have been developed [3], and space borne missions optimized for ocean color have been proposed.

The spectral diffuse reflectance of the natural waters (the "ocean color") is proportional to the ratio of the backscattering (b_b) coefficient to the absorption coefficient (a), i.e., b_b/a [4]. High spectral resolution absorption data are available for particles suspended in natural waters, but there is no instrumentation available to provide high spectral resolution backscattering data. Such data are needed to understand the hyperspectral diffuse reflectance of natural waters, for both interpretation and for modeling of hyperspectral data. In this paper we provide examples of the derivation of high resolution spectra of a and b_b from hyperspectral depth profiles of downwelling irradiance and upwelling radiance obtained in oligotrophic and mesotrophic waters, via methods of inverse radiative transfer [5,6].

We start by reviewing radiative transfer, defining the inherent and apparent optical properties of natural waters, and describing the inversion algorithm used to retrieve the inherent optical properties from the apparent optical properties. Next we describe the hyperspectral radiance/irradiance data and present the resulting inherent optical properties. Then we show how Raman scattering contamination limits the spectral range of applicability of the inversions. Finally, we provide a discussion of the results and some concluding remarks.

2. Radiative transfer, inherent and apparent optical properties

Consider a plane parallel, vertically stratified water-body with the z-coordinate measured from zero at the surface downward. Let the direction of propagation of light be specified by the unit vector $\hat{\xi}$, defined as follows. With the x-y plane parallel to the water surface, let $\hat{e}_x$, $\hat{e}_y$ and $\hat{e}_z$ be unit vectors in the x, y, and z directions, respectively. Then $\hat{\xi}$ is given by

$$\hat{\xi} = \hat{e}_x \sin\theta\cos\varphi + \hat{e}_y \sin\theta\sin\varphi + \hat{e}_z \cos\theta,$$

where θ is the angle between the propagation direction and the + z axis, and ϕ is the azimuth angle in the x-y plane. The radiative transfer (RT) equation for radiance $L(z,\hat{\xi})$ propagating in the direction $\hat{\xi}$ in the medium is [7]

#113277 - $15.00 USD Received 24 Jun 2009; revised 14 Aug 2009; accepted 21 Aug 2009; published 27 Aug 2009

$$\hat{\xi} \bullet \hat{e}_z \frac{\mathrm{d}L(z,\hat{\xi})}{\mathrm{d}z} = -c(z)L(z,\hat{\xi}) + \int\limits_{all\ \hat{\xi}'} \beta(z,\hat{\xi}' \to \hat{\xi})L(z,\hat{\xi}')\,\mathrm{d}\Omega(\hat{\xi}'),$$

where $c(z)$ is the beam attenuation (extinction) coefficient of the medium and $\beta(z,\hat{\xi}' \to \hat{\xi})$ is the volume scattering function (differential scattering cross section per unit volume) for scattering from the direction $\hat{\xi}'$ to the direction $\hat{\xi}$. Although not specified in the argument lists, all quantities also depend on the wavelength λ of the radiation. The quantity $\mathrm{d}\Omega(\hat{\xi}')$ is the differential solid angle surrounding $\hat{\xi}'$, and the integration is carried out over the entire range of solid angles. The total scattering coefficient $b(z)$ is given by

$$b(z) \equiv \int\limits_{all\ \hat{\xi}'} \beta(z,\hat{\xi}' \to \hat{\xi})\,\mathrm{d}\Omega(\hat{\xi}'),$$

and the absorption coefficient $a(z)$ by

$$a(z) = c(z) - b(z).$$

An important quantity in ocean color remote sensing is the backscattering coefficient defined through

$$b_b(z) \equiv \int\limits_{all\ \hat{\xi}\bullet\hat{\xi}'\le 0} \beta(z,\hat{\xi}' \to \hat{\xi})\,\mathrm{d}\Omega(\hat{\xi}').$$

The quantities $a(z)$, $b(z)$, $c(z)$, and $\beta(z,\hat{\xi}' \to \hat{\xi})$ are termed the inherent optical properties (IOPs) of the medium. It is convenient to define a normalized function, the scattering phase function, $P(z,\hat{\xi}' \to \hat{\xi})$, to specify the dependence of scattering on direction, according to

$$P(z,\hat{\xi}' \to \hat{\xi}) = \frac{\beta(z,\hat{\xi}' \to \hat{\xi})}{b(z)}.$$

It is independent of the magnitude of the scattering. The IOPs are linearly summable over those of the water and of the constituents suspended or dissolved in the water, e.g.,

$$\beta(z,\hat{\xi}' \to \hat{\xi}) = \beta_w(z,\hat{\xi}' \to \hat{\xi}) + \beta_p(z,\hat{\xi}' \to \hat{\xi}),$$

where the subscripts "w" and "p" refer, respectively, to water and suspended particles. For convenience later, we define component IOPs, some of which are directly amenable to measurement with existing *in situ* instruments. The absorption coefficient a is separated into that due to water, particles, and dissolved material, denoted respectively by the subscripts "w", "p", and "g", respectively: $a = a_w + a_p + a_g$. Likewise, $b = b_w + b_p$, $b_b = b_{bw} + b_{bp}$, $c = c_w + c_p + c_g$, $a_{pg} = a_p + a_g = a - a_w$, and $c_{pg} = c_p + c_g = c - c_w$.

In contrast to IOPs, radiometric quantities derived from the radiance in the medium, e.g., the downward propagating irradiance

$$E_d(z) \equiv \int\limits_{\hat{\xi}\bullet\hat{e}_z>0} \hat{\xi} \bullet \hat{e}_z L(z,\hat{\xi})\,\mathrm{d}\Omega(\hat{\xi}),$$

the upward irradiance

$$E_u(z) \equiv \int\limits_{\hat{\xi}\bullet\hat{e}_z<0} |\,\hat{\xi} \bullet \hat{e}_z\,| L(z,\hat{\xi})\,\mathrm{d}\Omega(\hat{\xi}),$$

and the scalar irradiance

#113277 - $15.00 USD Received 24 Jun 2009; revised 14 Aug 2009; accepted 21 Aug 2009; published 27 Aug 2009

$$E_0(z) \equiv \int_{all\ \hat{\xi}} L(z,\hat{\xi})\, \mathrm{d}\Omega(\hat{\xi}),$$

are termed apparent optical properties (AOPs). Other AOPs derived from these are the radiance reflectance

$$R_L(z) = \frac{L_u(z)}{E_d(z)},$$

where $L_u(z)$ is the radiance propagating toward the zenith, i.e., in the $-z$ direction, the various irradiance attenuation coefficients

$$K_x(z) = -\frac{\mathrm{d}\ell n E_x(z)}{\mathrm{d}z},$$

where $x = d$, u, or 0, and the average cosine

$$\bar{\mu}(z) = \frac{E_d(z) - E_u(z)}{E_0(z)}.$$

In a homogeneous water body, $R_L(z)$, $K_x(z)$, and $\bar{\mu}(z)$ are all only weakly dependent on depth; hence they are termed "apparent" optical properties. Of course they are not properties of the medium alone because they depend on the external illumination, e.g., the solar zenith angle, as well.

If the RT equation is multiplied by $\mathrm{d}\Omega(\hat{\xi})$ and integrated over all directions $\hat{\xi}$, the result can be put in the form

$$a(z) = \bar{\mu}(z)\, K_V(z),$$

where

$$K_V(z) = -\frac{\mathrm{d}\ell n\left(E_d(z) - E_u(z)\right)}{\mathrm{d}z}.$$

This *exact* relationship is referred to as Gershun's equation.

Given the IOPs and the distribution of radiance incident on the medium, it is possible to show [8] that the solution to the RT equation is unique as long as $a(z) \neq 0$, which is always the case if the medium (or part of the medium) is water. In the case of interest here, the medium is the ocean-atmosphere system illuminated by the solar beam; hence the actual IOPs will yield a unique solution to the radiance.

3. The inversion algorithm

The inversion algorithm is a procedure for the retrieval of $a(z)$ and $b_b(z)$ from the downwelling $E_d(z)$ and upwelling $E_u(z)$ irradiances. As in the present application, when the upwelling radiances $L_u(z)$ are measured rather than $E_u(z)$, the code retrieves $Q(z) = E_u(z)/L_u(z)$ as well. The inversion algorithm is described in detail in Gordon and Boynton [5].

The basic idea of the inversion algorithm is to use the measured AOPs to find IOPs that reproduce the AOPs when inserted into the RT equation. This is effected through an iterative procedure in which trial IOPs are introduced into the RT equation, which is then solved for the AOPs. Based on the differences between the measured and calculated AOPs, a new trial set of IOPs is determined and the RT equation solved again, etc. Gordon and Boynton [5] found that their method of varying the IOPs usually "converges" to a solution. However, one must not be too ambitious, as the AOPs depend only weakly on $b(z)$ but strongly on $a(z)$ and $b_b(z)$ [9]. Thus, neither $b(z)$ nor $c(z)$ can be obtained except in rare situations: when the scattering phase function of the particles is known *a priori*. Although $E_d(z)$ and $L_u(z)$ are input

#113277 - $15.00 USD Received 24 Jun 2009; revised 14 Aug 2009; accepted 21 Aug 2009; published 27 Aug 2009

into the code, the AOPs that actually drive the solution are $K_d(z)$ and $R_L(z)$. $E_d(z)$ and $L_u(z)$ are usually measured by independent sensors. Their absolute calibration is unimportant; however, because of the importance of $R_L(z)$, the relative calibration of $E_d(z)$ and $L_u(z)$ is of paramount importance.

The solution to the RT equation (at each iteration) requires a guess for the scattering phase function; Gordon and Boynton [5] however showed that the accuracy of the guess was not crucial, and that excellent retrievals could still be obtained with an incorrect phase function. Indeed, if the phase function actually used in the retrievals is close to being correct, then excellent retrievals of both $b(z)$ and $c(z)$ are obtained as well. Usually, the algorithm is operated with a depth-independent phase function. However, in clear water there is a considerable contribution to β from β_w, particularly into the backward hemisphere. This can cause significant variations in the phase function with depth in a stratified medium, and this degrades the performance of the algorithm. Thus, the following modification to the algorithm was developed [6]. A fixed phase function was first chosen for the *particles*, and then the algorithm was operated to completion resulting in $a(z)$ and $b_b(z)$. From $b_b(z)$ and the phase function, $b(z)$ can be computed, along with the fraction $\eta(z) = b_w/b(z)$. Then the phase function is modified to

$$P(z,\hat{\xi}' \to \hat{\xi}) = \eta(z) P_w(\hat{\xi}' \to \hat{\xi}) + \left(1-\eta(z)\right) P_p(\hat{\xi}' \to \hat{\xi}),$$

where $P_w(\hat{\xi}' \to \hat{\xi})$ is the phase function for pure water, and $P_p(\hat{\xi}' \to \hat{\xi})$ is the depth-independent phase function for particles. This new depth-dependent phase function was then used in the RT code and after operating the full algorithm with the modified phase function, new values of $a(z)$ and $b_b(z)$ were obtained, which yield new estimates of $\eta(z)$, etc. We call these iterations on $\eta(z)$ "external" iterations to differentiate between the iterations in the Gordon and Boynton [5] algorithm which we refer to as "internal" iterations. Boynton and Gordon [6] showed that this procedure yielded retrievals in clear water at the accuracy seen earlier in the constant-P_p algorithm. In the results presented in Section 5, up to a maximum of 50 internal iterations were employed and 6 external iterations were used.

This algorithm has the attribute that it provides IOPs that reproduce the AOPs as accurately as possible; however, if the physics used to relate the AOPs and IOPs is incomplete, the retrieved IOPs will be incorrect, although the reconstructed irradiances will be excellent. As Raman scattering and fluorescence are important, particularly at longer wavelengths, they should be included; however, here we ignore both transspectral terms, but assess the influence of Raman scattering on the final results in Section 6.

4. The data sets

The hyperspectral AOP data we examine here consist of depth profiles of the downwelling spectral irradiance, E_d, and the upwelling spectral radiance toward the zenith, L_u, measured at 3.3 nm increments from 350 to 700 nm with a wavelength accuracy of ± 0.1 nm. Each spectral band was approximately 9 nm wide. The data were obtained at two locations. The first station was approximately 12 miles west of the north coast of Lanai, Hawaii in oligotrophic waters (Chl *a* ~0.1 mg/m^3) occupied during February/March, 2007, and the second station was approximately 11 miles west of San Diego, California in mesotrophic waters (Chl *a* ~1 mg/m^3) and occupied in January, 2008.

The measured values of E_d and L_u as a function of depth and wavelength at the Hawaii station are provided in Figs. 1 and 2, respectively. These were obtained using a free-fall profiling radiometer system (HyperPro II, Satlantic Inc.). Sensors were characterized and calibrated using National Institute for Standards and Technology (NIST) standard lamps pre- and post- cruise following standard protocols developed in partnership with NASA and NIST (e.g., [10,11]). For the Hawaii experiment, sensors were intercompared with NIST-provided standards of spectral irradiance and radiance at the field site as well. Based on these

#113277 - $15.00 USD Received 24 Jun 2009; revised 14 Aug 2009; accepted 21 Aug 2009; published 27 Aug 2009

documented results, absolute radiometric uncertainty is assessed at < 2.8% for radiance, and < 2.1% for irradiance.

Dark corrections are made using an internal optical shutter operated throughout each profile. An above-water downwelling irradiance sensor mounted in the ship's superstructure is used to ensure stable surface values as the profile is taken, and tilt and temperature measurements are made using sensors onboard the instrument. Measured radiometric quantities are corrected for out-of-band stray light and thermal responsivity.

During data processing, all raw sensor data are first converted into engineering units using the calibration coefficients, and corrected for dark values, stray light and thermal responsivity. Quality control procedures include elimination of data with instrument tilts > 5°, and any profiles with significant fluctuations in surface irradiance due to clouds. Data from the radiance and irradiance sensors are then interpolated to common depth and wavelength bins, and referenced to absolute depth by way of surface pressure tare values.

To avoid clutter on the graphs in Figs. 1 and 2, only the data at approximately 6 nm intervals from 353 to 552 nm are plotted (every other wavelength is omitted). Noting that the algorithm requires vertical derivatives of E_d and L_u, some data smoothing is required. The smoothing for the Hawaii data was effected by computing a running average of these quantities taken over 11 m (the value at z is taken to be the average of the values obtained from z – 5 m to z + 5 m). For the San Diego station, the data were smoothed over a depth of 5 m.

Examination of the E_d profiles shows that near the surface in some parts of the profiles the irradiance actually increases with depth. Such artifacts are likely due to surface waves. The inversion algorithm cannot handle such occurrences, so these regions must be omitted from the inversion. For the Hawaii station, the depth range actually used was 20 to 90 m, while for the San Diego station the range was 5 to 19 m. The maximum depth at each station is restricted to ensure that retrievals at all wavelengths cover the same depth range.

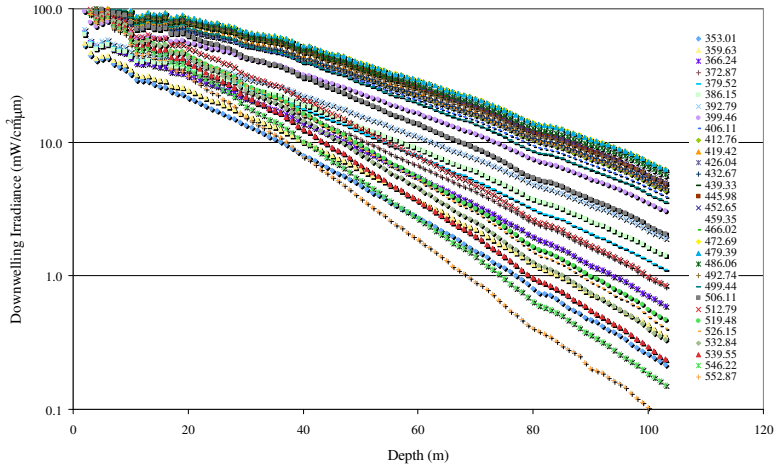

Fig. 1. Vertical profiles of E_d off Lanai, Hawaii. Legend: wavelength in nm.

#113277 - $15.00 USD Received 24 Jun 2009; revised 14 Aug 2009; accepted 21 Aug 2009; published 27 Aug 2009

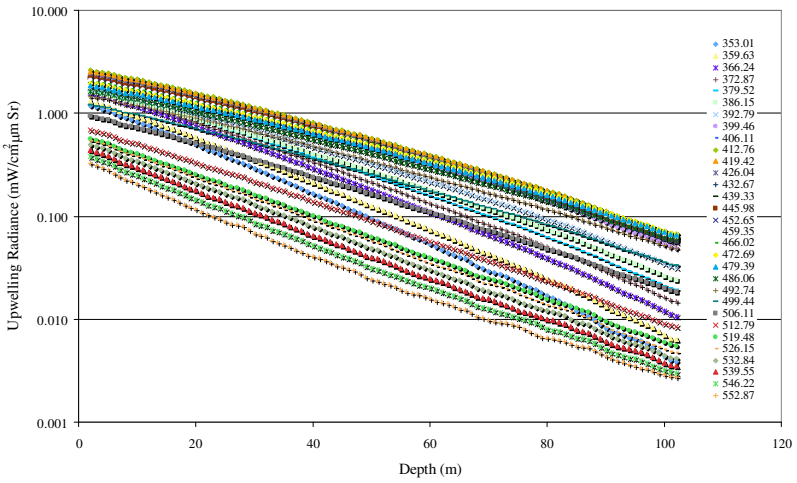

Fig. 2. Vertical profiles of L_u off Lanai, Hawaii (same location as Fig. 1).

Contemporaneous *in situ* data were obtained providing $a_{pg}(z)$ and $c_{pg}(z)$ at the Hawaii station using an ac-9 (WET Labs, Inc.). A purified water blank (Barnstead Nanopure 4-cartridge water purification system) was obtained with the ac-9 following the protocol of Twardowski et al. [12] 2 days before the presented *in situ* data were collected to quantify any drift from the manufacturer's calibration. Corrections for time lags, the temperature and salinity dependence of pure water absorption and attenuation [13,14], and drift were applied in post-processing. Scattering errors associated with the reflective tube absorption measurement [15] were obtained independently by convolving directly measured volume scattering functions with the scattering error weighting function presented in McKee et al. [16] for the ac-9 reflective tube. Volume scattering functions were measured at 10° increments with a prototype device called the MASCOT [17].

Measurements with an ECO-BB3 (WET Labs, Inc.) provided $b_b(z)$ at 462, 527, and 657 nm. For each wavelength, a single measurement of broadly weighted scattering in the backward direction, centered at 124°, is made. The sensor was calibrated with NIST-traceable, 0.2 µm microspherical beads (Duke Scientific) according to the method of Twardowski et al. [18]. A correction for absorption of incident and scattering beams was applied [18,19], but had a negligible effect (<1%). Backscattering coefficients were obtained from these measurements of scattering by first subtracting $\beta_w(124°)$ using the pure water backscattering values of Zhang and Hu [20] with salt effect added according to Zhang et al. [21]. The resulting particulate fraction $\beta_p(124°)$ was used to compute b_{bp} according to the relationship $b_{bp} = 2\pi\, \chi_p(124°)\, \beta_p(124°)$ [22,23], where $\chi_p(124°)$ was set to 0.89 following the empirical analysis by Sullivan et al. [24] for the ECO-BB sensors. After Berthon et al. [25], the χ_p was assumed to be spectrally invariant. Pure seawater backscattering, b_{bw} [20,21], was then added to b_{bp} to obtain total backscattering, b_b. At 527 nm, b_{bw} was approximately 60% of b_b in surface waters.

At the San Diego station *in situ* data were obtained providing $a_{pg}(z)$, $a_g(z)$, $c_{pg}(z)$, $a_p(z)$, and $c_p(z)$ along with $b_b(z)$ at 527 and 657 nm. Consecutive casts were made with the same ac-9 with and without a 0.2 µm prefilter to obtain the "*g*" component and "*pg*" components, respectively. The "*p*" components were obtained by difference. An ECO-BB2C (WET Labs, Inc.) was used for the $b_b(z)$ measurements, following the protocol used for the ECO-BB3 deployed for the Hawaii station. At 527 nm, b_{bw} was approximately 25% of b_b near the surface. The data acquired with these state-of-the-art *in situ* instruments is considered to constitute a validation data set for the inversion retrievals.

#113277 - $15.00 USD Received 24 Jun 2009; revised 14 Aug 2009; accepted 21 Aug 2009; published 27 Aug 2009

5. Results

We now describe the results of the inversion for the two data sets.

5.1 The Hawaii data set

The inversion algorithm was operated with the smoothed $E_d(z)$ and $L_u(z)$ data along with the wavelength and solar zenith angle. The Petzold phase function [7,26] was used for the particles. It was assumed that the atmosphere was aerosol free. (If aerosols are included, their influence is to decrease $E_d(z)$ and $L_u(z)$ by the same fraction; hence they have little or no influence on the resulting a and b_b. Simulations we carried out suggest that increasing the aerosol optical depth at 500 nm from zero, as assumed in these retrievals, to 0.25, which is actually high for a marine environment, will cause the retrieved values of a and b_b to increase by about 1%.) Figs. 3 and 4 provide the retrieved profile of a at 443 nm and b_b at 462 nm,

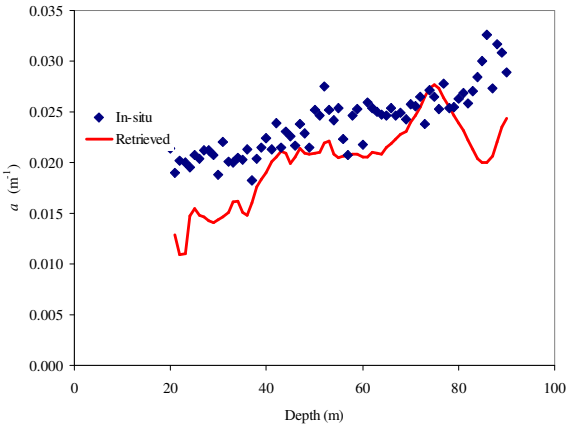

Fig. 3. Comparison of retrieved and *in situ* vertical profiles of absorption at 443 nm at the station off Lanai, Hawaii.

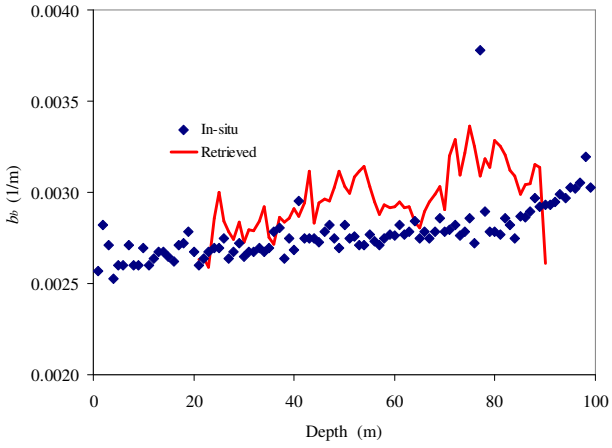

Fig. 4. Comparison of retrieved and *in situ* vertical profiles of backscattering at 462 nm at the station off Lanai, Hawaii.

#113277 - $15.00 USD Received 24 Jun 2009; revised 14 Aug 2009; accepted 21 Aug 2009; published 27 Aug 2009

respectively. These retrievals were typical of those over the entire spectrum. The depth variations of $a(z)$ follow almost exactly the depth variations of K_d. Also provided on Figs. 3 and 4 are the *in situ* measurements of $a(z)$ and $b_b(z)$ made with the ac-9 and ECO-BB3, respectively. The IOP data were averaged over 1 m depths to reduce noise. Overall, Fig. 3 suggests that the retrieved and *in situ* $a(z)$ are in excellent agreement for most of the profile, with no obvious trend with depth, except that the retrieved is usually smaller than the *in situ*. The differences are remarkably small, and usually less than ± 0.004 m^{-1}, within the (worst case) stated accuracy of the ac-9 instrument (± 0.005 m^{-1}).

In the case of $b_b(z)$ at 462 nm (Fig. 4), there are still obvious small-scale depth variations that correlate with the inversion-retrieved a. The figure shows that there is again a bias in the $b_b(z)$ results with the *in situ* values being ~0.0002 m^{-1} or less below the inversion-retrieved results. Clearly, the inversion-retrieved b_b increases at a slightly faster rate with depth than its *in situ* counterpart. This is likely due to the increasing importance of Raman scattering with depth at this wavelength (see Section 6).

To present the spectral distribution of the retrieved IOPs, we averaged the inversion retrievals over a depth range 20 to 90 m at each wavelength and compared them with similarly-averaged values of the *in situ* measurements. These are provided in Fig. 5 along with a_w and b_{bw}. Two representations of the absorption of pure water a_w are provided. The first ("Water Absorption – F") is taken from Sogandares and Fry [27] for the spectral region 340-380 nm and Pope and Fry [28] for 380-700 nm. However, there is evidence that, in both Refs. 27 and 28, a_w is overestimated for $\lambda \leq 420$ nm [29]. For this reason, we include a second estimate of a_w suggested by Morel et al. [29] in this spectral region ("Water Absorption – M"). The backscattering of pure seawater is taken from Zhang and Hu [20] and Zhang et al. [21]. The corresponding values of a_{pg} and b_{bp} are provided in Fig. 6. The retrieved quantities are remarkably smooth functions of wavelength and clearly display some of the spectral features of pure water. In particular, the absorption due to the seventh harmonic of the O-H stretching mode near 449 nm [28] is clearly revealed in the inversions (Fig. 5). In addition, the overall spectral variation in b_b is clearly dominated by the water itself. The inversion-retrieved absorption coefficient falls below that of pure water at wavelengths greater than 510 nm. Similarly b_{bp} near 490 nm (Fig. 6) departs from its spectral behavior at shorter wavelengths and begins to increase rapidly into the green region of the spectrum. This is due to the influence of Raman scattering (Section 6). The retrieved a_{pg}

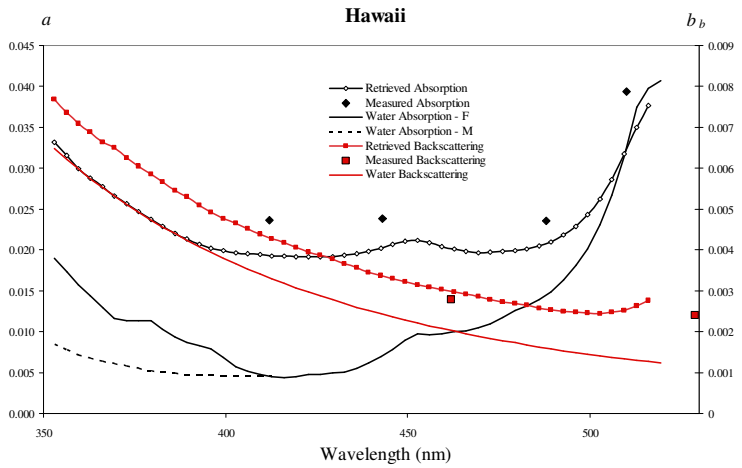

Fig. 5. Retrieved absorption (left scale) and backscattering (right scale) coefficients (in m^{-1}) for waters off Lanai, Hawaii. The retrieved quantities are averaged from 20 to 90 m.

#113277 - $15.00 USD Received 24 Jun 2009; revised 14 Aug 2009; accepted 21 Aug 2009; published 27 Aug 2009

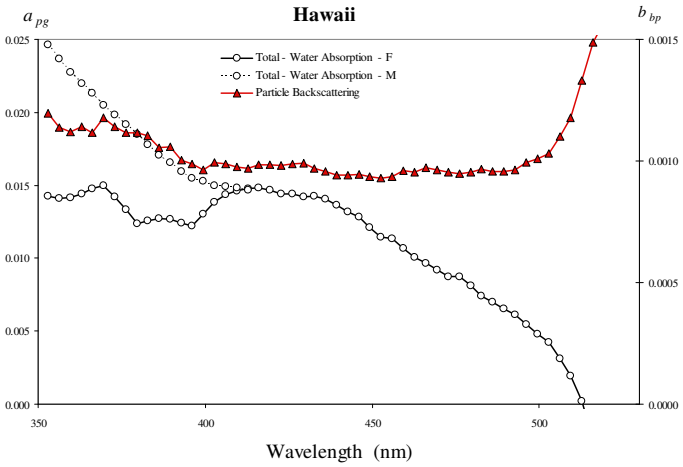

Fig. 6. Same data as Fig. 5 but with the absorption and backscattering of pure seawater removed.

shows absorption similar to that characteristic of phytoplankton; however, when "Water Absorption – F" is used for a_w, strange inexplicable features are seen between 350 and 400 nm. In contrast, when "Water Absorption – M" is used for a_w, the spectrum is smooth and displays an exponentially increasing absorption with decreasing wavelength in the UV characteristic of detrital particles and/or dissolved organic material. This suggests that a_w given in Ref. 29 more faithfully describes the absorption of water in the UV.

The backscattering coefficient appears to be more-or-less featureless in Fig. 6. Many investigators suggest that $b_{bp} \sim \lambda^{-n}$, e.g., Maritorena et al. [30]. Fitting b_{bp} to such a power-law over the range λ = 350 to 450 nm (to minimize the Raman contribution, longer wavelengths were omitted in the fit) we find n = 0.97 with an R^2 of 0.87.

5.2 The San Diego data set

The retrievals for the San Diego data are presented in Fig. 7. These are mean values of

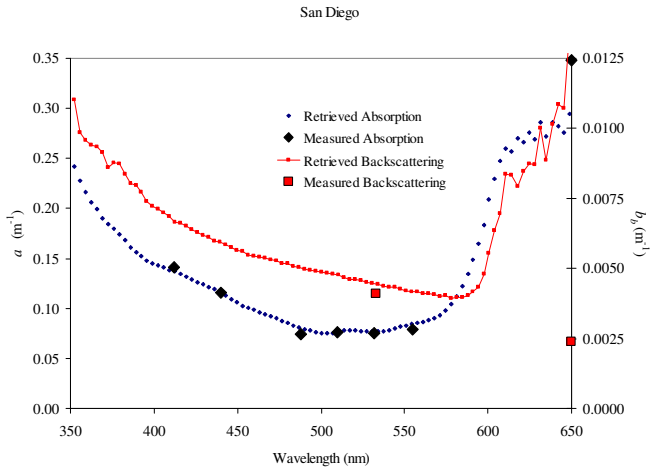

Fig. 7. Retrieved absorption (left scale) and backscattering (right scale) coefficients for waters off San Diego. The retrieved quantities are averaged from 5 to 19 m. The measured backscattering plotted at 650 nm is really that at 657 nm.

#113277 - $15.00 USD Received 24 Jun 2009; revised 14 Aug 2009; accepted 21 Aug 2009; published 27 Aug 2009

absorption and backscattering for the depth range 5 to 19 m. At wavelengths near 530 nm it is possible to carry out the retrievals to much greater depth; however, for presenting the full spectrum we again use averages over a common depth range. Figure 8 provides the absorption and backscattering coefficients of the water's constituents, $a_{pg}(\lambda)$ and $b_{bp}(\lambda)$,

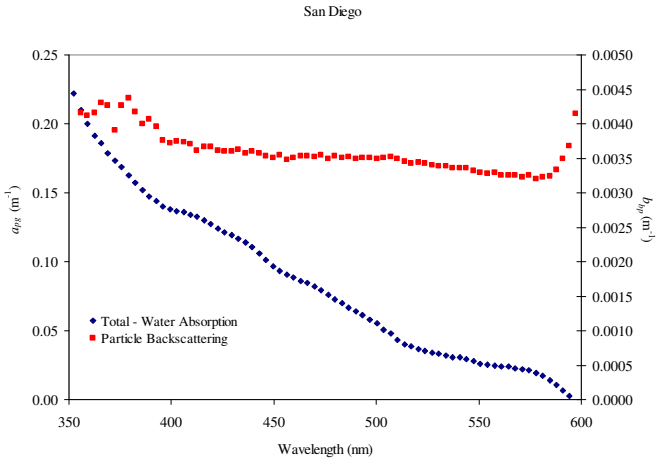

Fig. 8. Same data as Fig. 7 but with the absorption and backscattering of pure seawater removed.

respectively. We note that $a_{pg}(\lambda)$ becomes negative at about 595 nm, i.e., the retrieved $a(\lambda)$ becomes less than that of pure water. In addition, $b_{bp}(\lambda)$ near 590 nm begins to depart significantly from its weak decrease with increasing wavelength. As in the case of the Hawaii station, these effects are due to the increasing importance of Raman scattering as $a_w(\lambda)$ increases in this region. Clearly, the retrievals become poor at wavelengths somewhat less than 595 nm; however, Fig. 8 suggests that they should still be valid near 570 nm. For this data we find that $b_{bp} \sim \lambda^{-n}$ with $n \cong 0.40$ over the spectral range 400 to 570 nm.

We assess the influence of Raman scattering in the next Section with the aid of synthetic data, and show that reliable values of $a(\lambda)$ and $b_b(\lambda)$ can be obtained at wavelengths less than 575 nm at this station.

6. Effect of Raman scattering

The fact that the retrieved a becomes $< a_w$ at wavelengths ≥ 510 nm for the Hawaii station and ≥ 595 nm for the San Diego station, is manifest in the ever-increasing contribution of Raman scattering with increasing wavelength. In Raman scattering, photons at a wavelength $\lambda_e < \lambda$ are inelastically scattered to a wavelength, λ [31–34]. Assuming that the RT equation refers to radiance at a wavelength λ (the dependence of the radiance on λ was suppressed in Section 2), Raman scattering adds a term $J(z,\hat{\xi},\lambda)$ to the right-hand-side of the equation:

$$J(z,\hat{\xi},\lambda) = \iint\limits_{all\ \hat{\xi}',all\ \lambda_e} \beta_r(z,\hat{\xi}' \to \hat{\xi},\lambda_e \to \lambda) L(z,\hat{\xi}',\lambda_e)\, \mathrm{d}\Omega(\hat{\xi}')\, d\lambda_e$$

where the Raman scattering function β_r is given by

$$\beta_r(z,\hat{\xi}' \to \hat{\xi},\lambda_e \to \lambda) = \frac{3}{16\pi}\left(\frac{1+3\rho}{1+2\rho}\right)\left(1+\gamma(\hat{\xi}' \bullet \hat{\xi})^2\right) b_r(z,\lambda_e \to \lambda),$$

where ρ is the Raman depolarization (~0.17) and $\gamma = (1-\rho)/(1+3\rho)$. Note that

#113277 - $15.00 USD Received 24 Jun 2009; revised 14 Aug 2009; accepted 21 Aug 2009; published 27 Aug 2009

$$b_r(z,\lambda_e \to \lambda) = \int_{all\,\hat{\xi}'} \beta_r(z,\hat{\xi}' \to \hat{\xi},\lambda_e \to \lambda)\,\mathrm{d}\Omega(\hat{\xi}') = \int_{all\,\hat{\xi}} \beta_r(z,\hat{\xi}' \to \hat{\xi},\lambda_e \to \lambda)\,\mathrm{d}\Omega(\hat{\xi}).$$

As in the derivation of Gershun's equation, if we integrated J over solid angle we find

$$\int_{all\,\hat{\xi}} J(z,\hat{\xi},\lambda)\,\mathrm{d}\Omega(\hat{\xi}') = \int_{all\,\lambda_e} E_0(z,\lambda_e) b_r(z,\lambda_e \to \lambda)\,\mathrm{d}\lambda_e \cong E_0(z,\overline{\lambda}_e) \int_{all\,\lambda_e} b_r(z,\lambda_e \to \lambda)\,\mathrm{d}\lambda_e\,,$$

where $E_0(z,\lambda_e)$ inside the integral has been replaced by $E_0(z,\overline{\lambda}_e)$ outside the integral, with $\overline{\lambda}_e$ being the mean wavelength over the excitation band. This is acceptable because $E_0(z,\lambda_e)$ varies much more slowly with wavelength than $b_r(z,\lambda_e \to \lambda)$. The last integral has been found through laboratory measurements [35] to be

$$b_r(z,\lambda) = \int_{all\,\lambda_e} b_r(z,\lambda_e \to \lambda)\,\mathrm{d}\lambda_e = 2.61\times10^{-4}\left(\frac{589}{\lambda}\right)^{4.8\pm0.3}$$

where the wavelength is in nm. Thus, in the presence of Raman scattering, Gershun's equation for the absorption coefficient $a(z,\lambda)$ at λ becomes

$$a(z,\lambda) = \overline{\mu}(z,\lambda)K_V(z,\lambda) + \frac{E_0(z,\overline{\lambda}_e)}{E_0(z,\lambda)} b_r(z,\lambda)\,,$$

and if the last term is ignored, the retrieved absorption coefficient is too small. Although $b_r(z,\lambda)$ in the visible is small compared to $a(z,\lambda)$, at depths where the scalar irradiance ratio is large, i.e., $E_0(z,\lambda_e) >> E_0(z,\lambda)$, the influence of this term on $a(z,\lambda)$ can be significant. Note that at wavelengths where the contribution to Raman scattering is large, e.g., in the red, $\overline{\mu}(z,\lambda)$ and $K_V(z,\lambda)$ will differ significantly from the values that would be obtained in its absence, as in the inversion algorithm.

Although some corrections can be made for $a(z,\lambda)$ at Raman-compromised wavelengths using the above equation, there is no simple method for assessing the Raman-induced error in the retrieved absorption and backscattering coefficient. To provide an estimate of the error, we performed a series of RT simulations, using an RT code [34] that includes Raman scattering, in which the water's IOPs were similar to those measured or retrieved here.

6.1 The Hawaii station

For the Hawaii station, the simulations were carried out for λ = 412, 490, 510, and 556 nm, for which $\overline{\lambda}_e \approx 363,\ 420,\ 435$, and 471 nm. At wavelengths where the Raman contribution was expected to be small, λ < 510 nm, the depth-averaged retrieved values of the IOPs were used (along with the Petzold phase function for the particles). At wavelengths where the Raman contribution was expected to be large, i.e., 510 and 556 nm, the measured values of the IOPs were used (along with the Petzold phase function for the particles). For the purposes of computation of the Raman source function, J at λ, the Raman contribution to the light field at $\overline{\lambda}_e$ was assumed to be negligible (i.e., processes in which photons are Raman-scattered from $\lambda_a \to \lambda_b$ and again from $\lambda_b \to \lambda_c$, are ignored). These computations produced simulated values of $L_u(z)$ and $E_d(z)$ at each wavelength that were similar to those measured in the field. These simulated $L_u(z)$ and $E_d(z)$ values were then treated in a manner identical to the field data, i.e., entered into the inversion algorithm after smoothing, and the IOPs were retrieved. Contrary to the situation with field data, in the simulations we know the true values of all of the IOPs. The result of this exercise is presented in Table 1. As with the inversions presented in Fig. 5, the entries in the table for the inversions are averages over the depth range 20 to 90 m.

#113277 - $15.00 USD Received 24 Jun 2009; revised 14 Aug 2009; accepted 21 Aug 2009; published 27 Aug 2009

Table 1. IOPs and the differences between the true and inverted IOPs (in m^{-1}) averaged over 20 to 90 m for the simulated data set that included Raman scattering, but for which Raman scattering was ignored in the inversion, as a function of wavelength (in nm).

λ	$(a)_{true}$	Δa	δa (%)	$(b_b)_{true}$	Δb_b	δb_b (%)
412	0.0193	+ 0.0005	+ 2.6	0.00429	+ 0.00003	1.0
490	0.0210	– 0.0005	– 2.4	0.00260	+ 0.00013	5.0
510	0.0417	– 0.0024	– 5.8	0.00222	+ 0.00053	24.1
556	0.0639	– 0.0095	–14.9	0.00183	+ 0.00214	116.9

Key: $\Delta a = a_{inverted} - a_{true}$, $\delta a = (a_{inverted} - a_{true})/a_{true}$,
$\Delta b_b = (b_b)_{inverted} - (b_b)_{true}$, $\delta b_b = ((b_b)_{inverted} - (b_b)_{true})/(b_b)_{true}$,

Several conclusions are evident from these simulations. First, at wavelengths where Raman is not important (e.g., 412 nm), the accuracy of the inversion process is ~ ± 0.0005 m^{-1} for a and ± 0.00003 m^{-1} for b_b in waters with IOPs similar to those at the Hawaii station. (Note that these accuracies are for the quantities that are averaged over 20 to 90 m. The errors at a given depth will be ~8 times these, as borne out in Figs. 3 and 4.) Next, assuming the Raman induced error in b_b at 462 nm were equal to that at 490 nm (it is a little smaller), it could explain the somewhat faster increase in b_b with depth compared to the *in situ* data (if the mean Raman-induced error is + 0.00013 m^{-1}, then at z = 20 m one would expect it to be ~0, while at z = 90 m one would expect it to be ~0.00026 m^{-1}.). This suggests that the non-Raman induced bias in b_b at the Hawaii station is ~0.0001 to 0.0002 m^{-1}. Finally, if one were to extrapolate the b_b for wavelengths less than about 450-470 nm out to 510 nm, the difference between the extrapolated and inverted values would be approximately that given in Table 1.

6.2 The San Diego station

To examine the overall influence of Raman scattering on the San Diego retrievals, we created synthetic data (in the same manner as for the Hawaii station) with IOPs similar to those at the San Diego station. We then computed the elastic and Raman components of the in-water light field. The results suggested that Raman scattering could begin to become significant near 575 nm. Since the algorithm ignores Raman scattering we expect increased errors toward the red portion of the spectrum. Table 2 provides a comparison between the true and retrieved IOPs from 550 to 625 nm, the spectral region where Raman scattering will begin to invalidate the retrieved IOPs.

Table 2. IOPs and the differences between the true and inverted IOPs (in m^{-1}) averaged from 5 to 20 m, for the simulated data set that included Raman scattering, but for which Raman scattering was ignored in the inversion, as a function of wavelength (in nm). Key: Same as Table 1.

λ	$(a)_{true}$	Δa	δa (%)	$(b_b)_{true}$	Δb_b	δb_b (%)
550	0.0815	– 0.0001	– 0.1	0.00396	+ 0.00008	+ 2.0
575	0.0983	– 0.0002	– 0.2	0.00378	+ 0.00008	+ 2.1
600	0.2424	– 0.0115	– 4.7	0.00360	+ 0.00249	+ 81.7
625	0.3024	– 0.0259	– 8.6	0.00348	+ 0.00713	+ 204.8

These simulated retrievals confirm that the retrieved IOPs for the San Diego data should be unaffected by Raman scattering for wavelengths shorter than 575 nm. For waters with IOPs similar to the San Diego station, and in spectral regions in which Raman scattering is unimportant, these simulations suggest that under ideal conditions (e.g., the absence of environmental noise) the error in (the depth averaged) a and b_b should both be ~ ± 0.0001 m^{-1}.

#113277 - $15.00 USD Received 24 Jun 2009; revised 14 Aug 2009; accepted 21 Aug 2009; published 27 Aug 2009

7. Discussion

A shortcoming of our inversions is our inability to separate the absorption coefficient into its constituent parts. However, the *in situ* measurements of a_g allow the separation of dissolved absorption from particulate absorption. The a_g data at the San Diego station were found to fit an exponential function of wavelength: $a_g(\lambda) = a_g(\lambda_0)\exp[-S(\lambda_0 - \lambda)]$ with S = 0.0149 nm^{-1}. Over the range 412 to 555 nm the maximum difference between the measured and the exponential fit was 0.002 m^{-1}. To try to estimate a_p, we interpolated and extrapolated the exponential fit for a_g to the rest of the spectrum and subtracted it from a_{pg} (Fig. 8). The resulting a_p is provided Fig. 9. This procedure has rendered the absorption bands [2] of

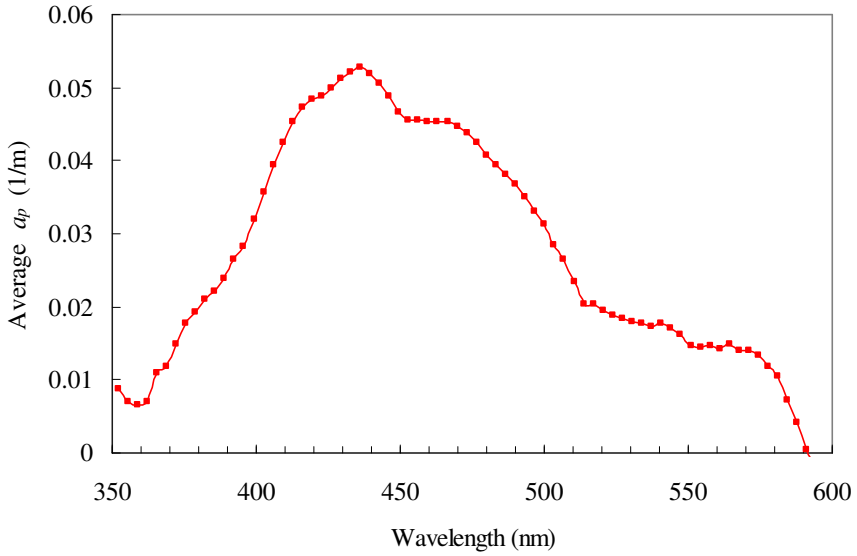

Fig. 9. Estimated absorption coefficient (averaged from 5 to 19 m) of particles for the San Diego station.

Chlorophyll *a* (382, 416 and 436 nm), Chlorophyll *b* and Chlorophyll *c* (466 and 462 nm, respectively), and Carotenoids (489 nm) clearly visible, and demonstrates that even in mesotrophic waters the in-water diffuse light field contains considerable information regarding the details of the pigmentation of the particles.

An important result of this study is the observation that the backscattering coefficient is almost void of any spectral features, i.e., the spectra confirm that to a good approximation $b_{bp} \sim \lambda^{-n}$. However, closer examination of Fig. 8 reveals that $b_{bp}(\lambda)$ appears to be slightly depressed over the spectral region attributed to phytoplankton (Fig. 9). It is well known that phytoplankton spectral absorption features are muted in spectra of the beam attenuation coefficient $c(\lambda)$. This implies that the spectral scattering coefficient must be depressed near absorption features (for several examples of spectra obtained for phytoplankton cultures, see Bricaud et al. [36], and for backscattering by particles in eutrophic waters, see Morel et al. [37]). This effect has been called anomalous dispersion [38,39], and results from the real part of the refractive index of a particle changing in the vicinity of an absorption band. The influence of anomalous dispersion on phytoplankton $b_{bp}(\lambda)$ was examined theoretically by Zaneveld and Kitchen [39], who predicted localized spectral depressions, particularly pronounced at wavelengths shorter than an absorption band peak.

#113277 - $15.00 USD Received 24 Jun 2009; revised 14 Aug 2009; accepted 21 Aug 2009; published 27 Aug 2009

If rather than fit $b_{bp}(\lambda)$ to a power law from 400 to 575 nm, we fit only the regions $\lambda \leq 399$ nm and $\lambda \geq 500$ nm, i.e., away from the dominant phytoplankton pigment absorption bands, we find $n = 0.595$ rather than the earlier 0.40. Taking this to be what the backscattering coefficients of the particles would be in the absence of the 400 to 500 nm particle absorption features, we can attribute the difference ($\Delta b_{bp}(\lambda)$) between the modeled $b_{bp}(\lambda)$ and the measured $b_{bp}(\lambda)$ to this depression effect. Figure 10 provides a comparison of $-\Delta b_{bp}(\lambda)$ and

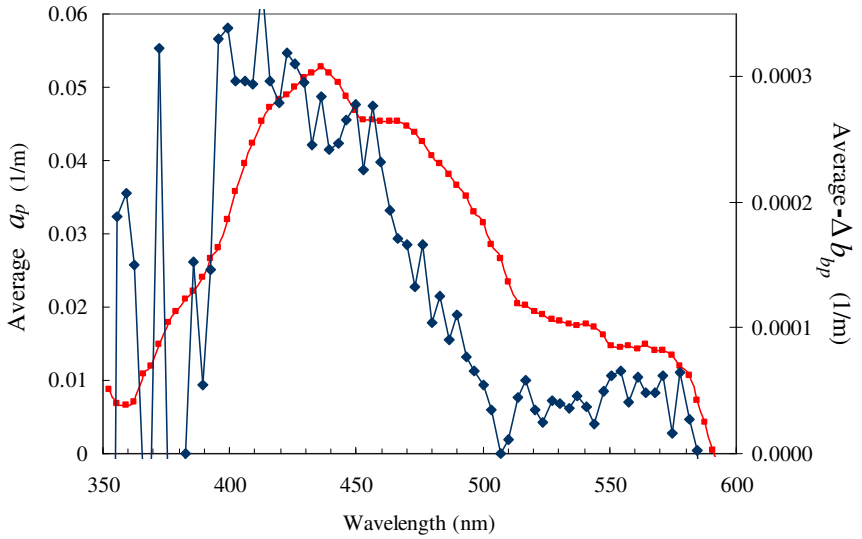

Fig. 10. Comparison between $-\Delta b_{bp}(\lambda)$ (right scale) and $a_p(\lambda)$ (left scale) indicating the depression of particle backscattering through the phytoplankton absorption bands.

$a_p(\lambda)$ showing a similar pattern between enhanced particulate absorption and depressed particulate scattering. It appears that the maximum depression of $b_{bp}(\lambda)$ is ~8-10%, and that this peak is blue-shifted relative to the maximum in absorption, consistent with the theoretical findings of Zaneveld and Kitchen [39].

Is it possible that the $b_{bp}(\lambda)$-depression observed is due to a tendency for the inversion algorithm to decrease $b_{bp}(\lambda)$ in the presence of enhanced a? To test this, a set of simulations at 450 nm were conducted in the following manner. The IOPs of the particles at the Raman excitation wavelength (390.3 nm) were held constant, while the IOPs of the particles at 450 nm were varied in such a manner that $c_p(450)$ was held constant. At this wavelength, $a_w = 0.00922$ m^{-1} and $b_w = 0.00454$ m^{-1}. The resulting retrievals are provided in Table 3. Clearly, as a varies at constant c, there is no tendency for a significant change in the accuracy of the retrievals. Furthermore, the magnitude of the depression (~0.0003 m^{-1}) is much larger than the inversion error for the simulated data set (Table 3). Thus, the depression of the backscattering in the absorption bands is not likely to be due to retrieval error.

Table 3. IOPs and the differences between the true and inverted IOPs (in m^{-1}) at 450 nm averaged from 5 to 20 m, for the simulated data set that included Raman scattering, but for which Raman scattering was ignored in the inversion. In this case c_p was held constant as a_p varies. Key: Same as Table 1.

λ	$(a)_{true}$	Δa	δa (%)	$(b_b)_{true}$	Δb_b	δb_b (%)
450	0.08622	+ 0.00040	+ 0.46	0.005732	– 0.000006	– 0.10
450	0.09622	+ 0.00056	+ 0.58	0.005551	– 0.000012	– 0.28
450	0.10622	+ 0.00052	+ 0.49	0.005370	0.000000	0.00
450	0.11622	+ 0.00018	+ 0.15	0.005189	+ 0.000049	+ 0.94
450	0.12622	+ 0.00008	+ 0.05	0.005007	+ 0.000009	+ 0.18

#113277 - $15.00 USD Received 24 Jun 2009; revised 14 Aug 2009; accepted 21 Aug 2009; published 27 Aug 2009

Finally, it remains to examine the spectrum of the particle backscattering probability $\tilde{b}_{bp} \equiv b_{bp} / b_p$. This is possible only for retrieval wavelengths for which the ac-9 measurements are available (to provide b_p): 412, 443, 488, 510, and 555 nm. For the Hawaii station the spectral average $\tilde{b}_{bp}$ (in %) was 2.53 ± 0.10 over the range 412-488 nm, while for the San Diego station it was 1.022 ± 0.05 for 412-555 nm. At both stations there was little or no spectral variation (the ± values listed are the spectral extremes of the retrievals). The San Diego results (mesotrophic) are in good agreement with the determination of Morel et al. [37] for eutrophic waters (spectral average: 0.8%) and for yellow substance dominated Case 2 waters (1.25%). The high values of $\tilde{b}_{bp}$ for the Hawaii station (oligotrophic) likely indicate a greater proportion of small (possibly mineral) particles; however, because of the dominance of water in the backscattering at this station the results would be strongly influenced by any error in b_{bw}. In contrast, Twardowski et al. [18] found a high frequency of $\tilde{b}_{bp}$ values in the extremely oligothophic waters of the Southeast Pacific Ocean near 0.5%.

The retrieved values of $\tilde{b}_{bp}$ differ somewhat from that assumed in the inversion algorithm (1.81%). Although no detailed sensitivity study has been carried out, the inversion algorithms of the type presented here are generally rather insensitive to differences between the true and the assumed scattering phase function [5,6,40,41].

Concluding remarks

We believe this work demonstrates the potential power of hyperspectral measurements of AOPs, coupled with an inverse RT algorithm, to reveal high resolution spectral features of IOPs. This in turn opens a direct path to advanced spectroscopic analysis of both in situ and remotely sensed observations, including enhanced characterization of the composition of particle fields from space. In the case of backscattering, this is particularly important as high spectral resolution profiles of this quantity have, heretofore, been unavailable.

Acknowledgments

This research was carried out under NASA Contracts Numbers NNX06AD44G and NNX08AH93A (KJV, HRG), NNX06AH14G (MRL) and, NNX06AH86G (MST), as well as ONR Contract N00014-07-C0139 and NSERC (MRL, SDM). The retrieval algorithm was developed under ONR Grant Numbers N00014-97-1-0069 and N00014-99-1-0007 (HRG). Development of the MASCOT VSF sensor was supported under ONR code 322OE contract number N0001406C0027 (MST).

#113277 - $15.00 USD Received 24 Jun 2009; revised 14 Aug 2009; accepted 21 Aug 2009; published 27 Aug 2009